JOURNAL OF PROPULSION AND POWER
Vol. 27, No. 1, January–February 2011

Dynamics of a Longitudinally Forced, Bluff Body Stabilized Flame

Dong-Hyuk Shin,* Dmitriy V. Plaks,* and Tim Lieuwen†
Georgia Institute of Technology, Atlanta, Georgia 30318
and
Ulises M. Mondragon,‡ Christopher T. Brown,§ and Vincent G. McDonell¶
Energy Research Consultants, Laguna Hills, California 92653-1422

DOI: 10.2514/1.48056

This paper describes an investigation of the response of bluff body stabilized flames to harmonic oscillations. This problem involves two key elements: the excitation of hydrodynamic flow instabilities by acoustic waves, and the response of the flame to these harmonic flow instabilities. In the present work, data were obtained with inlet temperatures from 297 to 870 K and flow velocities from 38 to 170 m/s. These data show that the flame-front response at the acoustic forcing frequency first increases linearly with downstream distance, then peaks and decays. The corresponding phase decreases linearly with axial distance, showing that wrinkles on the flame propagate with a nearly constant convection velocity. These results are compared with those obtained from a theoretical solution of the *G*-equation excited by a harmonically oscillating, convecting disturbance. This kinematic model shows that the key processes controlling the response are 1) the anchoring of the flame at the bluff body, 2) the excitation of flame-front wrinkles by the oscillating velocity, 3) interference of wrinkles on the flame front, and 4) flame propagation normal to itself at the local flame speed. The first two processes control the growth of the flame response and the last two processes control the axial decrease observed farther downstream. These predictions are shown to describe many of the key features of the measured flame response characteristics.

Nomenclature

A	=	flame area
D	=	burner depth
d	=	bluff body width
f	=	frequency
f_o	=	forcing frequency
f_{BvK}	=	Bénard–von Kármán instability frequency
f_{KH}	=	Kelvin–Helmholtz frequency
G	=	isoscalar contour variable describing flame position
H	=	burner height
I_t	=	edge detection threshold
k	=	wave number
L	=	flame position
L'	=	fluctuation of flame position
$\lvert L'\rvert$	=	gain of Fourier transformed flame position
Q	=	heat release
R^2	=	goodness-of-fit parameter
Re	=	Reynolds number
S	=	distance along time-averaged flame front
S_L	=	laminar flame speed
S_T	=	turbulent flame speed
t	=	time
u	=	flow velocity in the x-direction
u'	=	unsteady axial flow velocity
u_0	=	mean flow velocity
$u_{c,\mathrm{eff}}$	=	effective convection velocity of a flame disturbance
$u_{c,v}$	=	convective velocity of a flow disturbance
u'_n	=	fluctuating flow velocity normal to the flame
$u_{t,0}$	=	mean flow velocity tangential to the flame
V	=	excitation voltage
v	=	flow velocity in the y-direction
W	=	burner width
x	=	position along mean flow direction
y	=	position perpendicular to mean flow direction
β	=	parametric flame-front angle
ε	=	nondimensionalized disturbance amplitude
θ	=	time-averaged flame-front angle
λ_c	=	convective wavelength, $=u_o/f_0$
ϕ_f	=	phase of a flame wrinkle
ϕ_x	=	phase of velocity perturbations in the x-direction
ϕ_y	=	phase of velocity perturbations in the y-direction
ω	=	disturbance radial frequency

Presented as Paper 2009-22 at the 47th Aerospace Science Meeting, Orlando, FL, 5–8 January 2009; received 9 November 2009; revision received 12 September 2010; accepted for publication 6 October 2010. Copyright © 2010 by Dong-Hyuk Shin, Dmitriy V. Plaks, Tim Lieuwen, Ulises M. Mondragon, Christopher T. Brown, and Vincent G. McDonell. Published by the American Institute of Aeronautics and Astronautics, Inc., with permission. Copies of this paper may be made for personal or internal use, on condition that the copier pay the $10.00 per-copy fee to the Copyright Clearance Center, Inc., 222 Rosewood Drive, Danvers, MA 01923; include the code 0748-4658/11 and $10.00 in correspondence with the CCC.

*Graduate Research Assistant, School of Aerospace Engineering, 270 Ferst Dr. Student Member AIAA.
†Associate Professor, School of Aerospace Engineering, 270 Ferst Dr. Senior Member AIAA.
‡Sr. Research Engineer, 23342 South Point Drive, Suite E.
§Research Manager, 23342 South Point Drive, Suite E.
¶Senior Scientist, 23342 South Pointe Dr, Suite E. Senior Member AIAA.

I. Introduction

THIS paper describes an investigation of the response of bluff body stabilized flames to harmonic oscillations. Prior studies have shown that this problem involves feedback between acoustic oscillations, hydrodynamic flow instabilities associated with the shear layer and wake, and unsteady heat release [1–4]. This problem involves two key elements: the excitation of hydrodynamic flow instabilities by acoustic waves, and the response of the flame to these harmonic flow instabilities, as illustrated in Fig. 1 [5]. These two elements are discussed briefly.

The bluff body flowfield consists of a boundary layer, a separated shear layer, and a wake [6]. The velocity field of the separated shear layer and the wake has an inflexion point, rendering both susceptible to hydrodynamic instabilities [7]. The wake mode, referred to here as the Bénard–von Kármán (BvK) instability, leads to alternate shedding of vorticity from opposite sides of the bluff body and a sinuous wake structure [8]. The frequency of this absolute instability (for a discussion of absolute vs convective instabilities, see Huerre and Monkewitz [9]), f_{BVK}, scales as u_o/D, where u_o and D denote the mean flow velocity and bluff body width, respectively [6]. The shear layer instability, or Kelvin–Helmholtz (KH) instability, is a convective instability associated with the amplification of disturbances, leading to vortex rollup and pairing of the separating shear

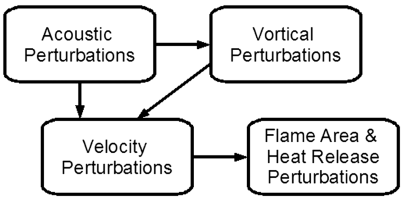

Fig. 1 Physical processes by which longitudinal and transverse flow oscillations lead to flame area (and hence heat release) oscillations.

layer [6,9]. The frequency of the most amplified KH instability mode is different from that of the BvK, because the relevant length scale is the shear layer thickness rather than the bluff body size. As such, the KH instability frequency is much larger than the BvK instability for high Reynolds number flows; e.g., relations from Prasad and Williamson [6] lead to $f_{\mathrm{KH}} = 0.0235^{*} f^{*}_{\mathrm{BVK}} Re^{0.67}$. Under the influence of harmonic excitation, the separated shear layer rolls up into vortices with a frequency commensurate with the frequency of excitation [10]. In addition, due to nonlinear interactions, velocity fluctuations occur at sum and difference frequencies of the forcing frequency and its harmonics [10]. As discussed in the next section, due to the apparent suppression of the BvK instability in flames with burned to unburned gas temperature ratios greater than about two [11], the shear layer instability is particularly critical in controlling the dynamics of acoustically excited, bluff body flames.

Heat release substantially influences the flow disturbances that are disturbing the flame [12–14]. Fundamental studies of vortex-flame interactions have shown that the nature of the flow changes substantially with the amplitude of vorticity perturbation [15–17]. For low vortex strengths, the flame is wrinkled with amplitude proportional to the ratio of u_θ/S_L, where u_θ denotes the velocity amplitude associated with the vortex and S_L the laminar flame speed. The amplitude of the vortex decreases through the flame due to volume dilatation and the large diffusivity of the products. Furthermore, if the flow and flame are nominally normal to each other, the baroclinic term is zero. As the amplitude of the vortex increases, the flame becomes highly wrinkled to the point that vorticity can also be produced/destroyed by baroclinic processes, i.e., very strong vortices distort the flame to such an extent that they change the sign of the baroclinically generated vorticity along the corrugated flame sheet. However, one key difference between the present investigation and the above-cited studies is the fact that the flame is nominally at an angle to the flow, so that baroclinic vorticity is present even in the nominal, unforced case. Nonetheless, this discussion illustrates the complications that can arise between shear-generated vorticity that has its own dynamics (e.g., rollup, pairing, growth, etc.), viscous diffusion, volume dilatation, and baroclinic processes.

The second element described in the first paragraph is the response of the flame to harmonic excitation. Substantial contributions have been made toward understanding the interaction between harmonic waves and premixed flames, and several issues have been identified as significant, such as stabilization dynamics and the spatial character of the disturbance field [18,19]. A number of prior studies have characterized the interaction of flames with harmonic waves arising due to both acoustic waves [20] and convecting, vortical disturbances [21,22]. The dynamics of the flame are controlled by flame kinematics, i.e., the propagation of the flame normal to itself at the local burning velocity, and the flowfield that the flame is locally propagating into. This is mathematically described by the so-called G-equation [23]:

$$\frac{\partial G}{\partial t} + \vec{u} \cdot \nabla G = S_L |\nabla G| \tag{1}$$

In this equation, the flame position is described by the parametric equation $G(\vec{x}, t) = 0$. Also, $\vec{u} = \vec{u}(\vec{x}, t)$ and S_L denote the flowfield just upstream of the flame and laminar flame speed, respectively. In the unsteady case, the flame is being continually wrinkled by the unsteady flowfield, $\vec{u}'$. The action of flame propagation normal to itself, the term on the right side of Eq. (1), is to smooth these wrinkles out. As such, a wrinkle created at one point of the flame due to a velocity perturbation propagates downstream and diminishes in size due to flame propagation.

The objective of this study is to characterize this relationship between acoustic, vortical, and flame sheet fluctuations. It extends prior measurements and analysis by the Georgia Tech group from lower velocity and Reynolds number situations to much higher velocity flames [24–26]. The next section describes the experimental facility and diagnostics. We then present analysis of these data, theoretical model predictions, and comparisons of data and the model.

II. Experimental Facility, Data Processing, and Modeling Approach

A. Experimental Setup and Data Postprocessing

Experiments are conducted in a premixed, atmospheric test rig (see Fig. 2a) operated in both a vitiated and nonvitiated mode [27]. The test section is 76.2 mm × 127 mm with a triangular bluff body that is 32 mm wide and 51 mm high (see Fig. 3). Air enters at the base of the setup and passes through a swirl stabilized natural gas burner. For nonvitiated test section operation, the burner serves to thoroughly mix the fuel and air. In the case of vitiated test section operation, the burner anchors the flame, which sits within the liner. The premixed fuel/air either continues along or is mixed with dilution air with varying preheat to allow oxygen content and temperature to vary independently. An extension section allows the generation of a uniform velocity and temperature distribution. For vitiated operation, natural gas is added immediately after the dilution section. The flow passes through a converging section and a honeycomb flow straightener before entering the test section. For the present work, the average flow velocity at the bluff body lip varies from 18 to 170 m/s and the inlet temperature into the test section varies from 297 (nonvitiated) to 870 K, see Table 1. The uncertainty in these flow velocities is ±5%.

Fuel concentration profiles were measured just upstream of the bluff body and spatial nonuniformities are less than 2% at 15 m/s and 20% at 190 m/s (the latter case is vitiated).

250 Hz longitudinal oscillations are excited with a driver section, installed upstream of the test section. These drivers consist of four 100 W Galls Speakers powered by two Samson Audio Servo 200 Power amplifiers. The signal is generated by a function generator. Acoustic measurements were obtained using a dynamic pressure transducer.

Flame dynamics are determined from direct flame luminosity, recorded with a Vision Research Phantom 7.2 black and white high-speed video camera. The visible (>330 nm) broadband light emission was recorded using a Nikon 35–70 mm zoom lens with an f-stop of 3.3. The exposure time was 310 ms and the recording rate was 3000 frames per second.

Particle image velocimetry (PIV) images were also obtained using Vision Research Phantom 7.2 high-speed video camera triggered externally by a 532 nm 12 Watt Coherent Prisma laser with varying laser intensity between 3.5 and 12 W. The vitiator air flow was seeded with a dry fluidized bed. The Al_2O_3 seed particles were introduced in the dilution air circuit. Mechanical shaking and ceramic balls were used to help break up agglomerates to an approximate D10 of 0.86–0.95 microns. In each experiment, 250 images were recorded at 20 kHz forming 249 PIV image pairs. An interrogation window of 32 × 32 pixels was chosen with a 50% overlap between windows producing a grid of 16 × 32 vectors per image.

B. Model Development

The basic approach used to model the flame dynamics is the level set, flame tracking approach. This approach is valid in the flamelet regime where the flame thickness is small relative to the hydrodynamic and acoustic length scales. In this experiment, the smallest disturbance wave length is $\sim 18\ \mathrm{ms}^{-1}/250\ \mathrm{Hz} = 72$ mm, much larger than the flame thickness. Moreover, no indications of local flame extinction were observed. This modeling approach is detailed

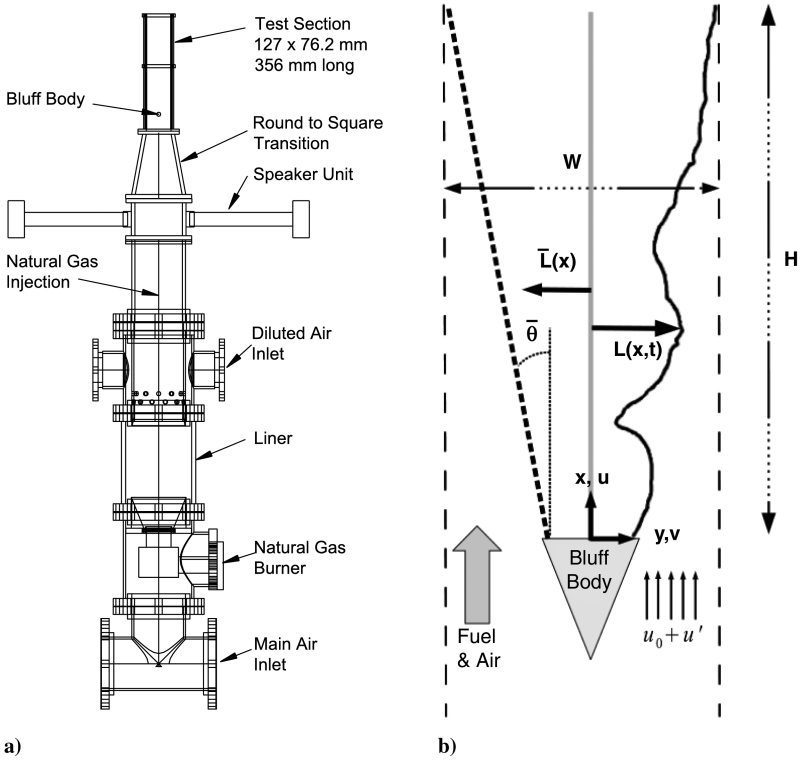

a) b)

Fig. 2 Schematics of a) the experimental rig, and b) flame model used to compare and predict experimental results. The left, dashed line indicates the time-averaged flame edge, while the right, solid line denotes the instantaneous flame location.

in Fleifil et al. [28], DuCruix et al. [29], Yang and Culick [30], and Lieuwen [31]. The flame position is modeled using the G equation, described in the Introduction section. Assuming that the flame position is a single valued function of the transverse coordinate, its instantaneous position L can be written as:

$$G(x, y, t) = L(x, t) - y = 0 \tag{2}$$

Thus, for a two-dimensional flame, the instantaneous flame position L is given by Shin et al. [32] (see Appendix for derivation):

$$\frac{\partial L}{\partial t} + u\frac{\partial L}{\partial x} - v = S_L\sqrt{\left(\frac{\partial L}{\partial x}\right)^2 + 1} \tag{3}$$

The coordinate system is shown in Fig. 2b. The G equation describes the spatial and temporal distributions of the flame position that can be related directly to the area. In this formulation, the effect of transverse and longitudinal velocity perturbations on the flame are captured through the (u, v) terms.

The G equation is a nonlinear partial differential equation with special properties, including being nonconservative and having the propensity to form discontinuities in derivatives. As such, special computational approaches are required for its solution. In particular, a robust numerical scheme is necessary which can accurately capture the formation of sharp gradients and cusps in the distorted flame front. The computational approach used here discretizes spatial derivatives using a weighted essentially nonoscillatory scheme developed for Hamilton–Jacobi equations [33]. This scheme is uniformly fifth-order accurate in space in the smooth regions and third-order accurate in discontinuous regions. Derivatives at the boundary nodes are calculated using fifth-order-accurate upwind-differencing schemes so that only the nodes inside the computational domain are used. A total variation diminishing Runge–Kutta scheme [34], up to third-order accurate, is used for time integration.

C. Image Processing

High-speed, line-of-sight movies were obtained of the acoustically forced flames. Typical images at several flow conditions are shown in Fig. 4. To determine the dynamics of the flame edge, given by $L(x, t)$ in Eq. (3), it is necessary to identify the location of the flame edges. This process is complicated by the integration over the line of sight in the image, which causes the edge of the flame in each

Table 1 Summary of flame luminosity experiments, flow conditions, and chosen threshold values. Each experiment was performed at 250 Hz excitation frequency at 6 and 12 V speaker excitation amplitudes

Air flow rate, kg/s	Air flow velocity at bluff body lip, m/s	Air flow temperature upstream of bluff body, K	Edge detection threshold
0.14	18	294	0.25
0.14	38	644	0.27
0.18	51	644	0.20
0.23	63	644	0.13
0.27	76	644	0.13
0.32	89	644	0.13
0.36	101	644	0.45
0.41	114	644	0.45
0.45	126	644	0.45
0.45	170	866	0.45

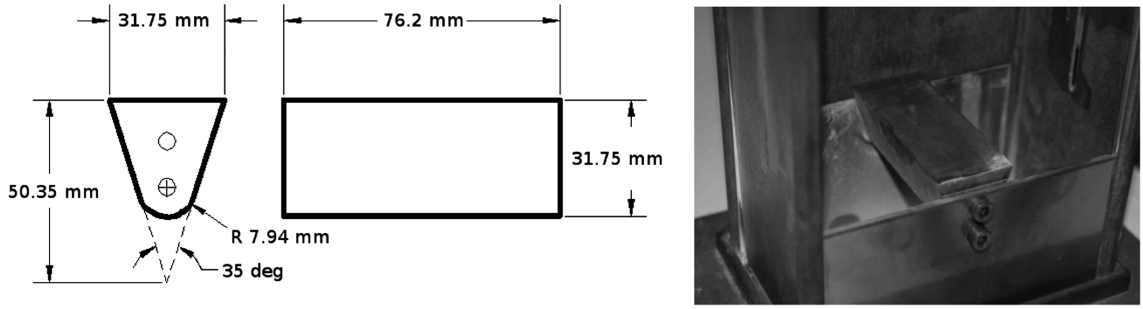

a) Design b) Installed in test section

Fig. 3 Schematic and photograph of bluff body used in these measurements.

image to grow increasingly diffuse with downstream distance due to the growing three dimensionality of the flame front.

These points can be seen in Fig. 5, which illustrates a typical flame image and transverse cuts of the smoothed intensity profile at two axial locations. Near the bluff body, an abrupt discontinuity in image intensity associated with the edge of the flame is observed. Farther downstream, this edge becomes increasingly diffuse. As such, the defined flame edge increasingly becomes a function of the threshold value (see discussion below) with downstream axial distance.

The specific procedure used for flame edge location is now discussed. First, the data is smoothed with a spatial low-pass filter. Since image intensity changes with downstream distance, the image is normalized to vary between zero and unity at each axial location. Then the flame edge, $L(x, t)$ is defined as the point where the intensity crosses a predefined threshold level, I_t. Note that two flame edges are extracted, associated with the right and left flame branches.

This process is repeated for all rows in a single image and again for all images in a movie and results in a time series for every axial location (x-direction), as shown in Fig. 6a. These time domain data are also converted into the frequency domain at each axial location by obtaining the Fourier transform of $L(x, t)$, see Fig. 6b. Note the spike at the forcing frequency, $f_0 = 250$ Hz. The resulting axial dependence of the flame response magnitude (magnitude of the FFT at the forcing frequency) and phase (phase of the FFT at the forcing frequency) are shown in Fig. 7. See also Fig. 10 in Sec. III for another illustration of this process.

To ensure a high quality of results, several techniques are used for checking data validity. First, each point in the time series is checked to make sure it lies further than 10 pixels away from the image border (due to the nature of the data and the edge detection algorithm, many erroneous points default to a value at the image border). If such a point is encountered away from top and bottom image boundaries (i.e., near the center of the flame), the gap is filled by interpolating between nearby points. The data is discarded when such events occur in the near field (starting with $x = 0$ and moving along the flame until a first valid point is encountered) of the bluff body and far downstream (starting at the top end of the image and moving down until a first valid point is encountered) where the magnitude of the fluctuations is low. Furthermore, the number of discontinuities and the mode of the time series are computed for each x-location. If the number of discontinuities is greater than 1.5% of the total number of points, the result is not reported. Further, the mode of the time series has to be within certain bounds or the result is not reported.

Second, the coherence between the left flame edge and the right flame edge is calculated at the forcing frequency. Only points where the coherence exceeds 0.9 are reported. Typical coherence data is shown in Fig. 8. It shows that coherence values are smallest near the bluff body and downstream, where the magnitude of flame sheet fluctuations is smallest and, therefore, random noise effects are most prominent. It also shows that coherence values generally increase as flow velocities decrease and as the amplitude of excitation increases.

The flame response magnitude, but not the phase, does depend upon threshold level, I_t. This sensitivity is illustrated in Fig. 9. Figure 9a shows the axial dependence of the flame response magnitude at the forcing frequency at several threshold values. It shows, as expected, that all results converge in the near field where the flame is nearly two dimensional. The curves diverge with downstream distance. Figure 9a also shows that low and high threshold values result in the largest and smallest magnitude of fluctuations, respectively. However, the curves have similar qualitative character, as will be discussed in the next section. Figure 9b shows the corresponding axial phase dependence and illustrates that phase is far less sensitive to threshold selection than magnitude, except in extreme cases.

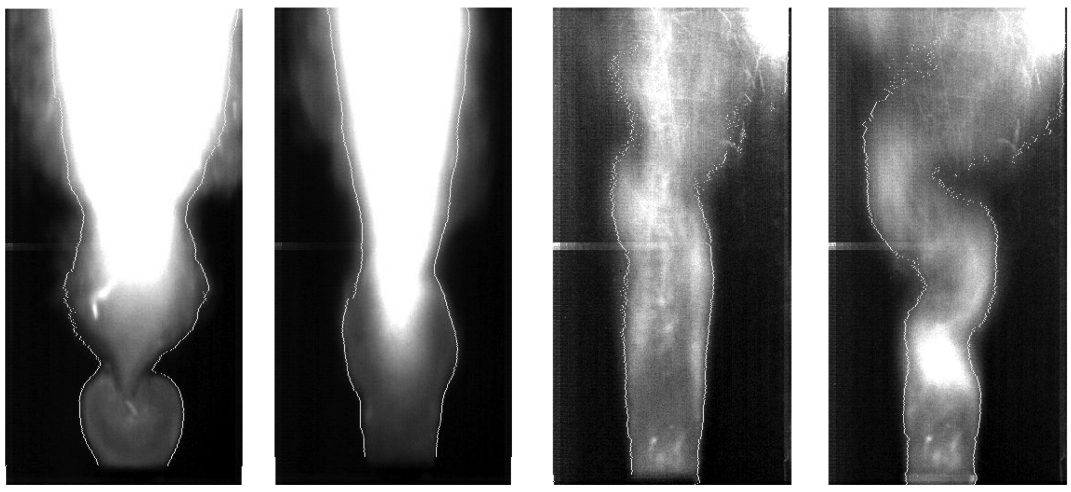

a) b) c) d)

Fig. 4 Luminosity flame images and their calculated edges at various flow conditions: a) 18.4 m/s, 294 K; b) 38.0 m/s, 644 K; c) 127 m/s, 644 K; d) 170 m/s, 866 K. All cases have a 12 V excitation voltage.

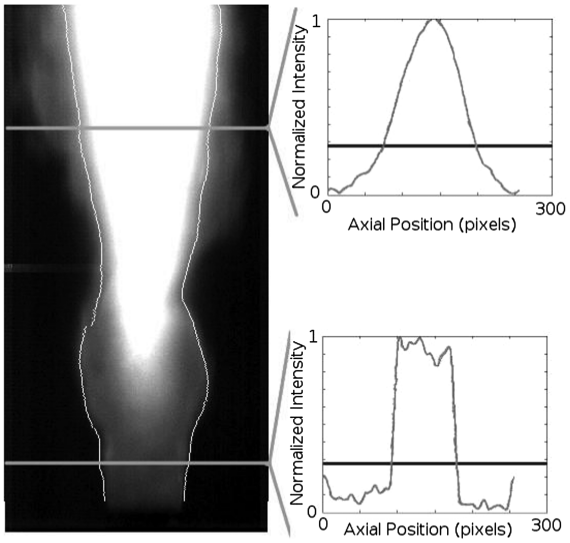

Fig. 5 Image intensity at two axial locations. The flame edge location is defined where the intensity (curve) crosses the threshold value (horizontal line), I_t. Flow velocity is 38.0 m/s at 644 K and 12 V excitation voltage.

For some flow conditions, I_t has little impact on the maximum flame edge response, while for other it is more sensitive to the threshold value choice. Results presented in the next section use different threshold values for different flow conditions, shown in Table 1, as each flow condition is optimized for best edge detection.

III. Experimental Results and Discussion

A. Luminosity Flame Response

Typical characteristics of flame-front position spectra (both amplitude and phase), under the influence of acoustic excitation are shown in Fig. 10. The convective wavelength, $\lambda_c = u_o/f_o$, (where u_o is the mean flow velocity at the bluff body lip) equals the distance a disturbance propagating at the mean flow velocity travels in one acoustic period and is an important length scale. Figure 10 shows the entire spectrum of the flame response at eight downstream locations. The envelope of the flame response at $f = f_o$ is also drawn. Close to the bluff body (located at $x/\lambda_c = 0$), the flame responds mainly at the frequency of excitation (f_o). Moving downstream, the response at $f = f_o$ first grows, reaches a maximum, and then decreases. This behavior is due to the growth and decay of the underlying flow structures as well as the propagation of the flame, which tends to smooth out the wrinkles. These results are quite similar to those observed from lower velocity flames [25]. The spectra also exhibit a monotonic increase in broadband fluctuations with downstream distance, i.e., the fluctuation level across all frequencies increases

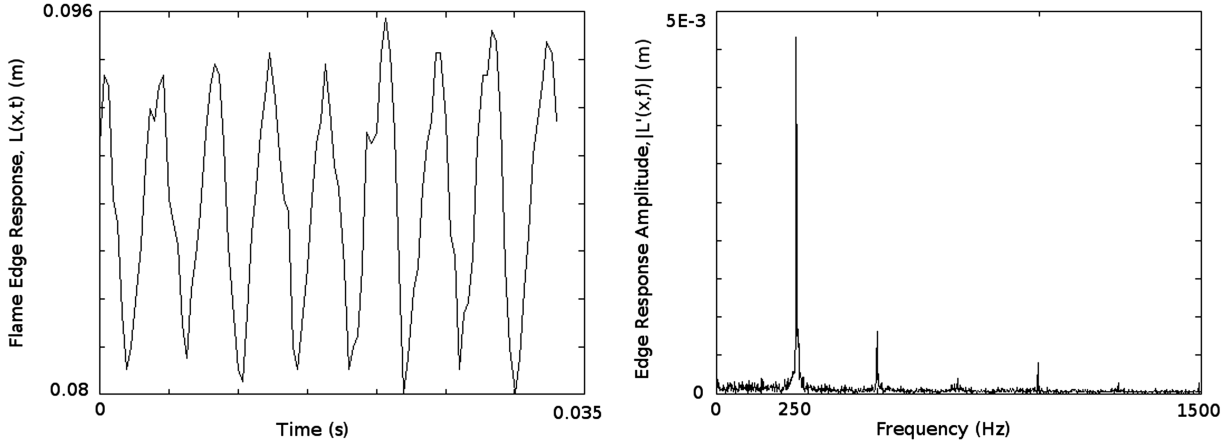

a) b)

Fig. 6 Part a) time series of flame position using $I_t = 0.27$ at axial location of $x/\lambda_c = 0.47$. Part b) corresponding spectrum, showing strong response at 250 Hz forcing frequency. Flow conditions: 38 m/s mean flow velocity, 644 K approach temperature, and 12 V excitation voltage.

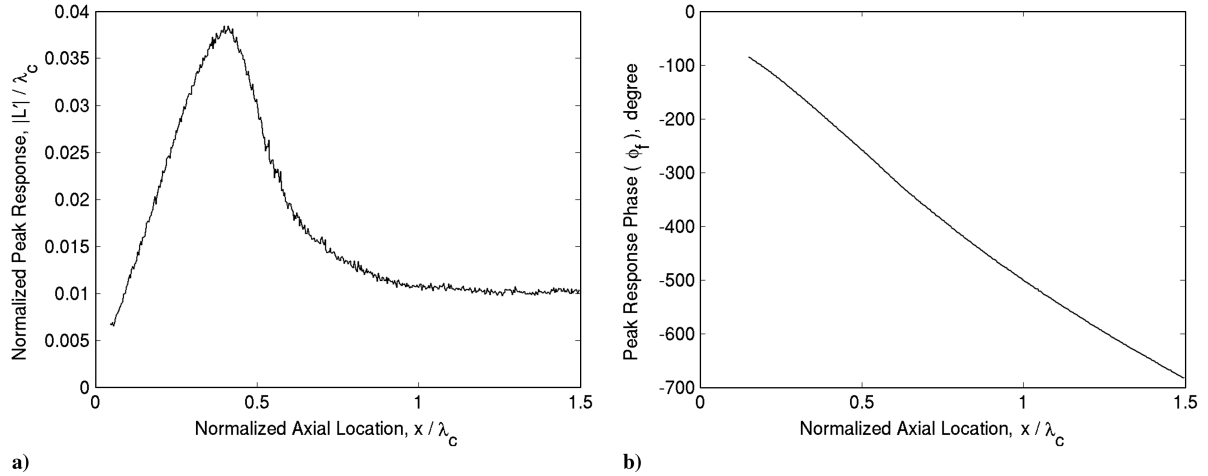

a) b)

Fig. 7 Normalized flame edge response amplitude (a) and phase (b) at the forcing frequency as a function of normalized downstream distance. Flame edge response amplitude, phase and downstream distance are normalized by the convective wavelength, λ_c. Flow conditions: 38 m/s mean flow velocity, 644 K approach temperature, 12 V excitation voltage and $I_t = 0.27$.

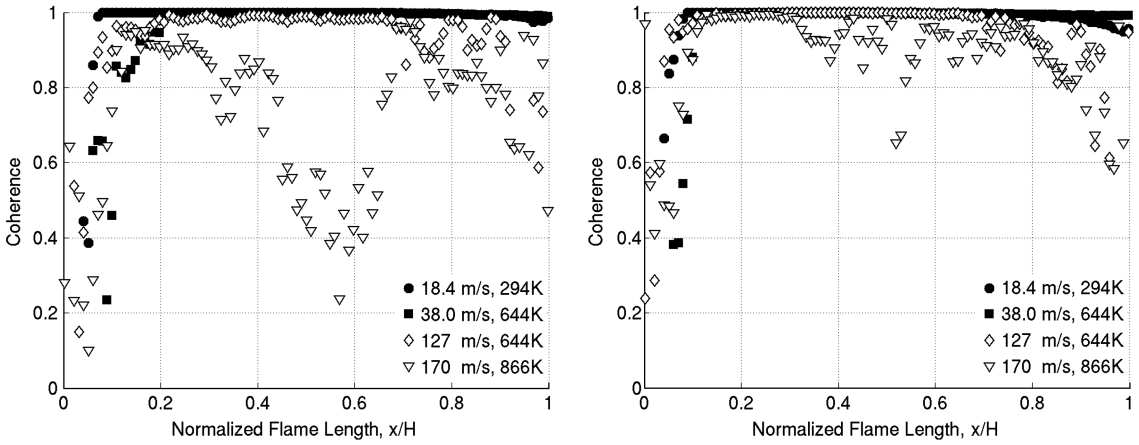

Fig. 8 Coherence of the left flame branch to the right flame branch at several flow conditions and a) 6 V and b) 12 V excitation voltage. Flow conditions: 38 m/s mean flow velocity, 644 K approach temperature.

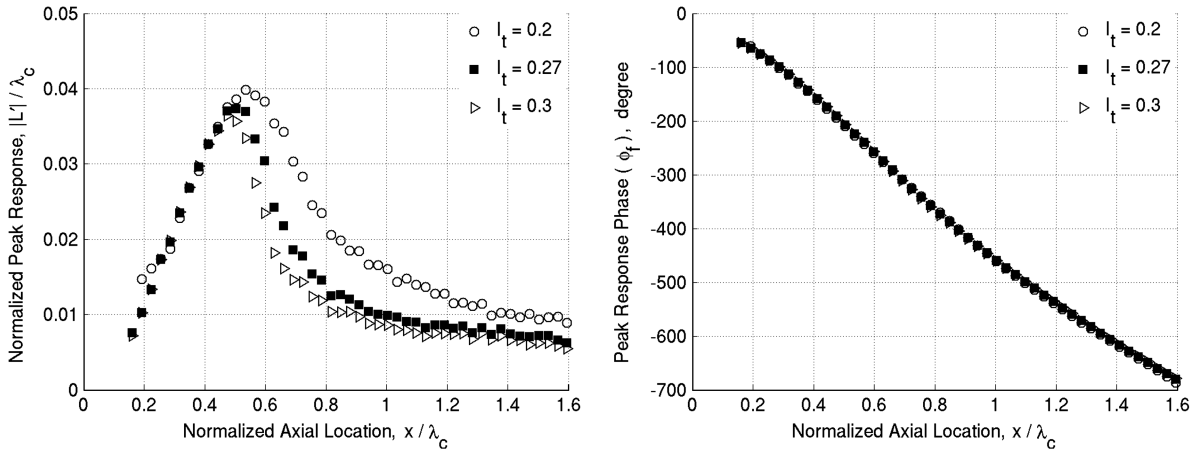

Fig. 9 Part a) dependence of flame edge response amplitude on threshold value, I_t. Part b) dependence of flame edge response phase on threshold value choice, I_t. Flow conditions: 38 m/s mean flow velocity, 644 K approach temperature, and 12 V excitation.

with downstream distance. This reflects the random flapping of the turbulent flame brush, which increases in magnitude with downstream axial distance.

Figures 11 and 12 overlay a number of similar plots at different velocities. Several important conclusions can be drawn from these results. Most significantly, all curves show essentially the same qualitative behavior for both gain and phase. The gain increases linearly in the bluff body near field, peaks farther downstream, and then decays. The decay rate varies strongly among the different curves; however its dependence upon I_t should be noted. The phase results are essentially on top of each other, showing that phase depends primarily upon downstream location and axial flow velocity (both effects captured in the parameter x/λ_c). The phase is referenced to its value at $x/\lambda_c = 0.2$ where good flame response occurs (flame response near $x = 0$ is very small, rending large phase uncertainties).

The strong effect of axial velocity in scaling the gain results should also be emphasized. In the lowest velocity cases, the entire axial dependence of the gain can be seen (rise, peak, then decay). At the highest flow velocities, only the spatial growth region is seen. This demonstrates that the appropriate axial viewing window necessary to completely characterize the flame's spatio-temporal dynamics increases linearly with flow velocity (and inversely with frequency, for related reasons).

Finally, by comparing the results for a given condition at two different excitation amplitudes, it can be seen that flame response increases with excitation amplitude although not necessarily in a linear manner. This can be seen from Fig. 13, which replots these same data, but normalizes the y-axis by amplitude of excitation. Note that the data collapses in the near field, but diverges in the far field.

B. Velocity Flowfield Measurements

This section describes the mean and perturbation flowfield, obtained using PIV measurements. Three quantities are of primary interest for comparisons of these results with theory: the mean axial

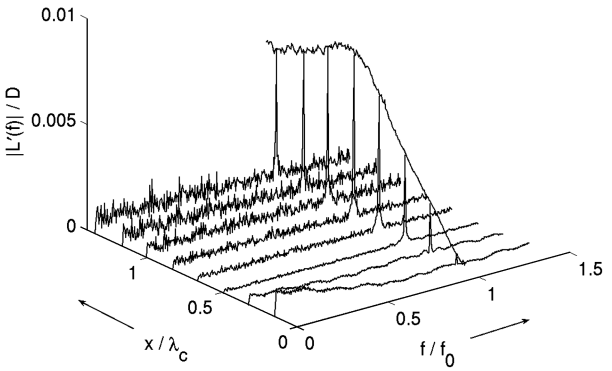

Fig. 10 Spectrum of flame sheet fluctuations, $L'(x,f)$ at different downstream locations (18.4 m/s, 294 K, 12 V excitation voltage). The x-coordinate is the downstream distance with $x = 0$ located at the bluff body trailing edge and f_o is the acoustic forcing frequency.

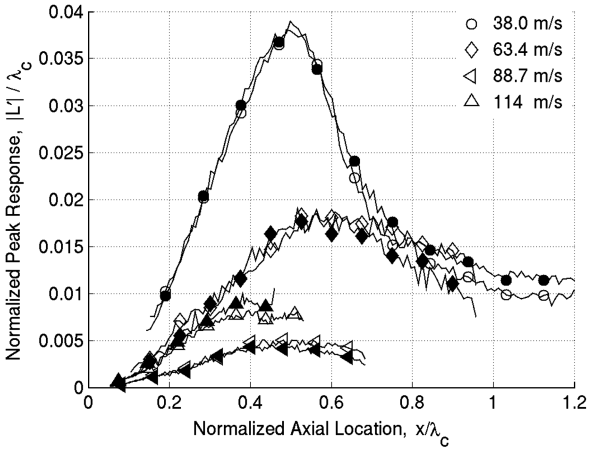

Fig. 11 Effect of flow velocity on peak flame response at 12 V excitation voltage at an inlet temperature of 644 K. The left flame edge is represented with filled-in symbols and the right flame edge is represented with open symbols.

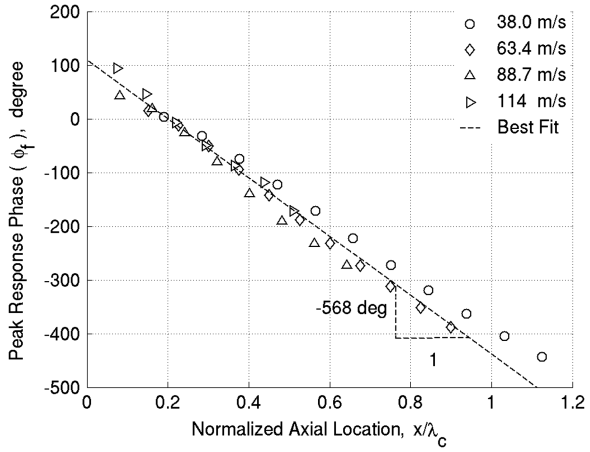

Fig. 12 Effect of flow velocity on phase at 12 V excitation voltage at an inlet temperature of 644 K. The x-coordinate is the downstream distance with $x/\lambda_c = 0$ located at the bluff body trailing edge. The best-fit line is a dashed line with the slope as indicated. The phase plots are referenced to $x/\lambda_c = 0.2$. Because the left and right flame edges have nearly identical phase, only the left flame edge phase is included here.

flowfield, transverse perturbation field amplitude, and axial convection velocity of the perturbations, $u_{c,v}$. These results were obtained from a time series of 249 images, representing three acoustic cycles. After subtracting the temporal mean, the flow response at the forcing frequency is determined by fitting the sum of two sine waves at frequencies of $f = f_o$ (the fundamental frequency) and $2f_o$ (the first harmonic) to the data. This procedure enables us to determine the local mean velocity u_0, amplitude of disturbance, $|u'|$ and $|v'|$, phase of flow disturbance, ϕ_x and ϕ_y, and goodness-of-fit parameter, R^2. Each experiment was repeated 5 times, producing five different realizations, which are averaged to reduce noise. Figure 14 show the instantaneous velocity at a point from the repeated measurements. These data show good repeatability. Figure 15a shows the time-averaged mean axial velocity. The mean axial velocity remains approximately constant outside of the recirculation zone for the entire length of the viewing window. Figure 15b plots the transverse velocity perturbation amplitude as a function of downstream distance. Some asymmetry in perturbation amplitude is evident.

C. Comparison with Model

The next discussion is on the solution characteristics of the G-equation. We start with a general overview of the linearized G-equation solution characteristics, given below, which provides important insight into key processes of excitation of flame wrinkles and their propagation along the flame in a wavelike manner (see also Appendix for derivation).

$$\frac{\partial L'}{\partial t} + \cos\theta \cdot u_{t,0}\frac{\partial L'}{\partial x} = \frac{u'_n}{\cos\theta} \tag{4}$$

As can be seen, the left side of the equation is a simple convection operator and describes the response of the flame to excitation at either the boundary (i.e., the flame attachment point) or along the flame (by the convecting vortical disturbances). In the absence of velocity fluctuation, u'_n, these flame wrinkles propagate along the flame at a speed given by

$$\text{if } u'_n = 0, \qquad u_{c,\text{eff}} = u_{t,0}\cos\theta \tag{5}$$

This equation is useful for understanding the phase dynamics of the flame response in the far-field where the vortical disturbance is dissipated.

The right side of Eq. (4) describes the excitation of the flame by the vortical disturbances. This vortical disturbance is also propagating in the axial direction at a velocity of $u_{c,v}$ which does not generally equal $u_{c,f}$. As such, the flame is continuously being locally perturbed by a disturbance moving at a speed of $u_{c,v}$, but the subsequent flame wrinkle then propagates downstream at a speed of $u_{c,f}$. This leads to interesting interference effects along the flame which have important

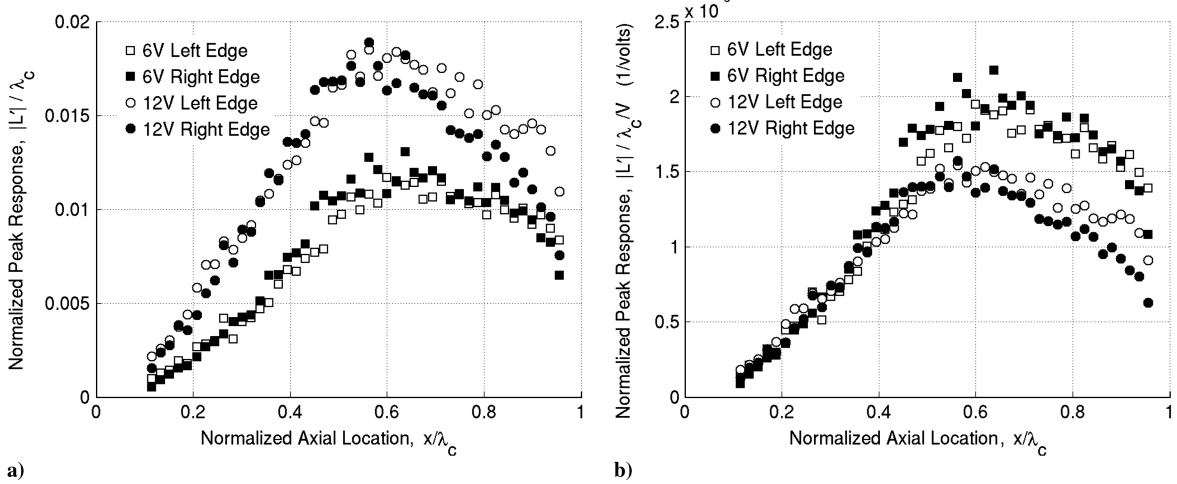

a) b)

Fig. 13 Normalized amplitude plot that compares two different excitation voltages at the same flow velocity of 63 m/s, with a) raw data and b) L' amplitude at forcing frequency normalized by speaker excitation voltage.

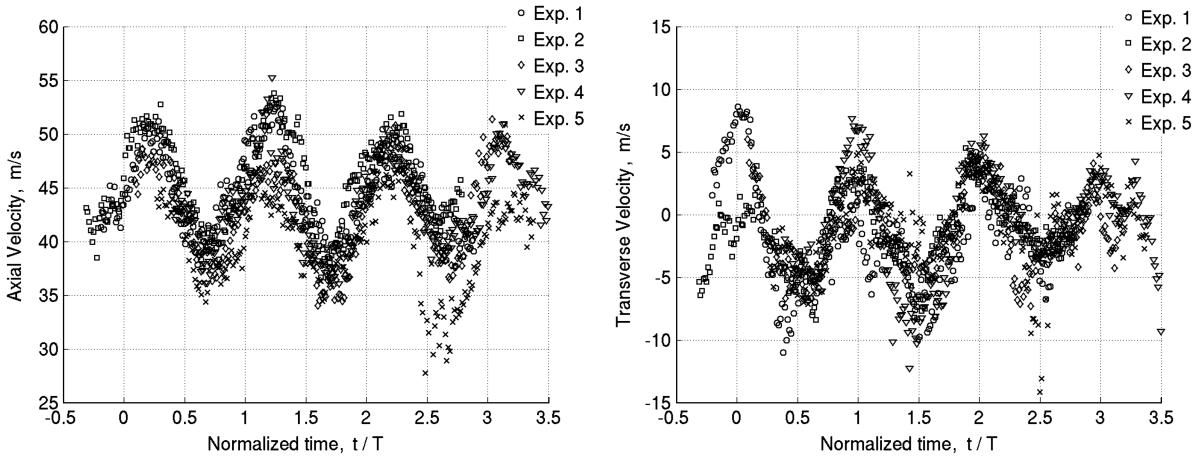

a) b)

Fig. 14 Time dependence of instantaneous velocity, from different realizations at $x/\lambda_C = 0.83, y/W = -0.45$. Time is normalized by the period of the forcing frequency, 250 Hz. Flow conditions: 38 m/s mean flow velocity, 644 K approach temperature, and 12 V excitation.

influences upon both the amplitude and phase evolution of the flame response. A key point here is that flame response is nonlocal in both space and time; i.e., wrinkling of the flame at a given axial location is due to disturbances at that point, but also disturbances excited at the boundary or along the flame at upstream locations and earlier times.

A key length scale is the convective wavelength, u_o/f_0. For low amplitude disturbances, $\varepsilon = v'/u_o \ll 1$, and/or small axial distance, $x/\lambda_c \ll 1$, nonlinear effects are negligible [29] and the linear and amplitude scaled nonlinear results converge, as illustrated in Fig. 13. However, for large ε or x/λ_c values, the flame wrinkles are damped out by flame propagation normal to itself. Linear calculations accurately describe the flame response features in the $x/\lambda_c \ll 1$ region, but nonlinear effects are needed to describe the flame response at large downstream distances. The rest of this section considers the different spatial regimes of flame response, closely following discussions in Shanbhogue et al. [25] and Shin et al. [32].

Consider first the initial growth region of the flame position magnitude. The initial increase in L' with x is due to flame anchoring; i.e., the flame attachment point remains largely fixed throughout the perturbation cycle. As such, the amplitude of L' must start at or near zero as shown in Fig. 16, which overlays a number of instantaneous realizations of the flame edge at different flow conditions.

The amplitude of L' then rises with downstream distance in response to the fluctuating velocity field. Even if the flame attachment point vibrates some, i.e., $L'(x = 0, t) \neq 0$, as long as the flame base does not move in phase and with the same amplitude as the flowfield, similar behavior occurs. Furthermore, because the amplitude of fluctuations in the $x \sim 0$ region is so small, nonlinear effects are negligible. These nonlinear effects are contained in the following term in Eq. (3), which describes flame propagation normal to itself.

$$S_L \sqrt{\left(\frac{\partial L}{\partial x}\right)^2 + 1} \tag{6}$$

In the near-field region, the flame dynamics near the attachment point are described by the linearized G equation. In this case, an explicit solution for the slope of the $|L'(x, f_o)|$ vs x can be derived in [25] (see Appendix for derivation):

$$\frac{\partial |L'(x=0,f)|}{\partial x} = \frac{|u'_n(x=0,f)|}{u_{t,0}(x=0)} \frac{1}{\cos^2\theta} \tag{7}$$

This equation assumes that $L'(x = 0, f) = 0$. It can be seen that the near-field flame response slope increases linearly with perturbation magnitude and is a function of flame angle (the nominal flame angle is $\sim 6^\circ$ from vertical, rendering the $\cos^2\theta = 0.99$, or essentially unity). This equation is important as it provides a closed form, explicit relationship between measured flame-front and flowfield properties. Specifically, it shows that the initial slope of the flame wrinkling amplitude is equal to the ratio of perturbation velocity amplitude normal to the flame, u'_n, divided by mean velocity tangential to the flame, $u_{t,0}$ and flame angle, $\cos^2\theta$. Again, because of the steep flame angle, these quantities are essentially equal to the

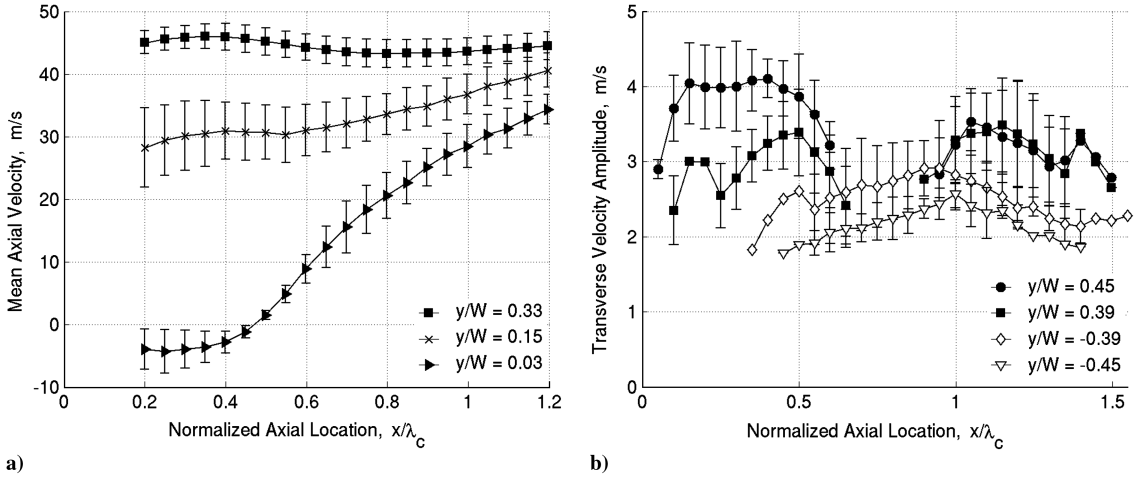

a) b)

Fig. 15 Axial dependence of a) time-averaged axial velocity and b) fluctuating transverse velocity amplitude. Error bars represent 1 standard deviation from five realizations. Mean velocity is 42 m/s, forcing frequency is 250 Hz, and amplitude of excitation is 12 Volts. Refer to Fig. 2b for coordinate system reference. The bluff body lip location is at $y/W = \pm 0.14$.

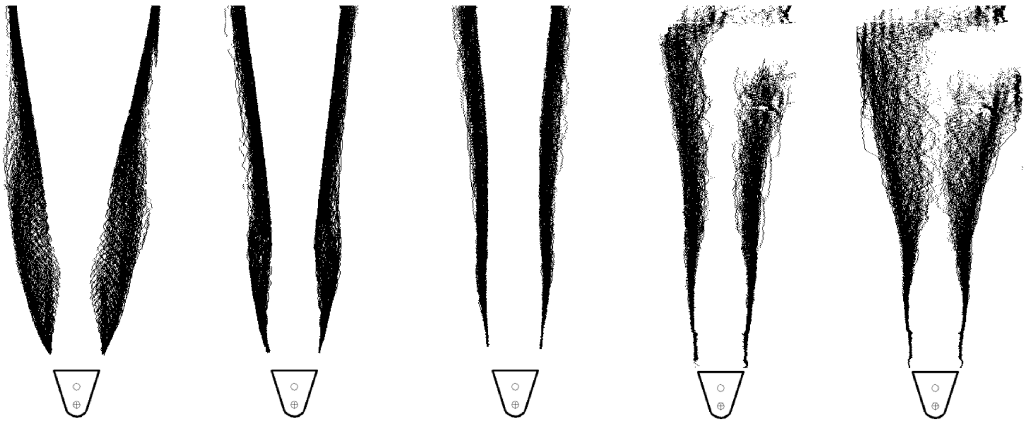

Fig. 16 Flame brush of 100 consecutive frames that demonstrate $L' \sim 0$ at $x = 0$ (bluff body trailing edge) for the following conditions: a) 18 m/s, 294 K; b) 38 m/s, 644 K; c) 76 m/s, 644 K; d) 126 m/s, 644 K; e) 170 m/s, 866 K and 12 V speaker excitation voltage. Note that bluff body placement in the above images is approximate.

transverse perturbation velocity and mean axial velocity, respectively.

The rest of this section focuses on comparisons with one experimental condition where flame and PIV data are both available, 38 m/s, 644 K and 12 V excitation voltage. To evaluate the theoretical result shown in Eq. (7), Fig. 17a overlays the measured flame position from one flow condition shown in Fig. 11 and a fit line. Using Eq. (7), the slope of this fit line can be used to estimate the value of $u_n'/u_{t,0} = 0.11$. This estimated value from the flame data is compared with the measured velocity results from the PIV data in Fig. 17b. Note that these two quantities are quite close, lying within the uncertainty of the velocity field measurements, and as such is an important validation of model predictions. This result shows how measured flowfield results can be used to make quantitative predictions on the spatio-temporal evolution of the flame front.

Measured and predicted phase characteristics are now compared. Again, in the near field, explicit solutions are possible using the linearized G equation (see Appendix for derivation).

$$\frac{1}{\omega}\frac{\partial \phi_f}{\partial x}\bigg|_{x=0} = -\frac{1}{2}\left(\frac{1}{u_{t,0}\cdot\cos\theta} + \frac{1}{u_{c,v}}\right) \tag{8}$$

Equation (8) assumes that $L'(x = 0, f) = 0$. Because of this boundary condition at $x = 0$, two equal magnitude but out of phase disturbances are excited at the flame attachment point, associated with the flame attachment boundary condition and the vortical disturbance, which propagate downstream at velocities of $u_{t,0}$, and $u_{c,v}$, respectively. Because of their equal magnitudes, they each contribute equally to the phase. Note that this phase slope can be written as an effective convection velocity of the flame wrinkle, $u_{c,\text{eff}}$:

$$\frac{1}{\omega}\frac{\partial \phi_f}{\partial x}\bigg|_{x=0} = -\frac{1}{u_{c,\text{eff}}} \tag{9}$$

As noted earlier, the effective convection velocity of flame wrinkle, $u_{c,\text{eff}}$, is not equal to the convection velocity of the vortex, $u_{c,v}$. Rather, it equals the harmonic mean of the projection of mean tangential velocity onto the x-coordinate, $u_{t,0}\cos\theta$, and of the flow perturbation convection speed, $u_{c,v}$. Note that the harmonic mean is always less than arithmetic mean, which sets the upper limit of the flame wrinkle convection speed, $u_{c,\text{eff}}$ in the near field. The near-field relationship between $u_{c,\text{eff}}$ and $u_{c,v}$ is given by:

$$\frac{u_{c,v}}{u_{c,\text{eff}}}\bigg|_{x=0} = \frac{1}{2}\left(\frac{u_{c,v}}{u_{t,0}\cos\theta} + 1\right) \tag{10}$$

Also, in the far field where the vortex is dissipated and the velocity excitation on the right side of the G equation, see Eq. (4), is gone, then $u_{c,\text{eff}} = u_{t,0}\cos\theta$, as shown in Eq. (5).

The above discussion shows the near and far-field limits of the convection speed of the flame wrinkle. In the near field, the flame wrinkle convection speed is the geometric mean of the vortical disturbance and the mean flow velocity. Near $x = 0$, it can be seen

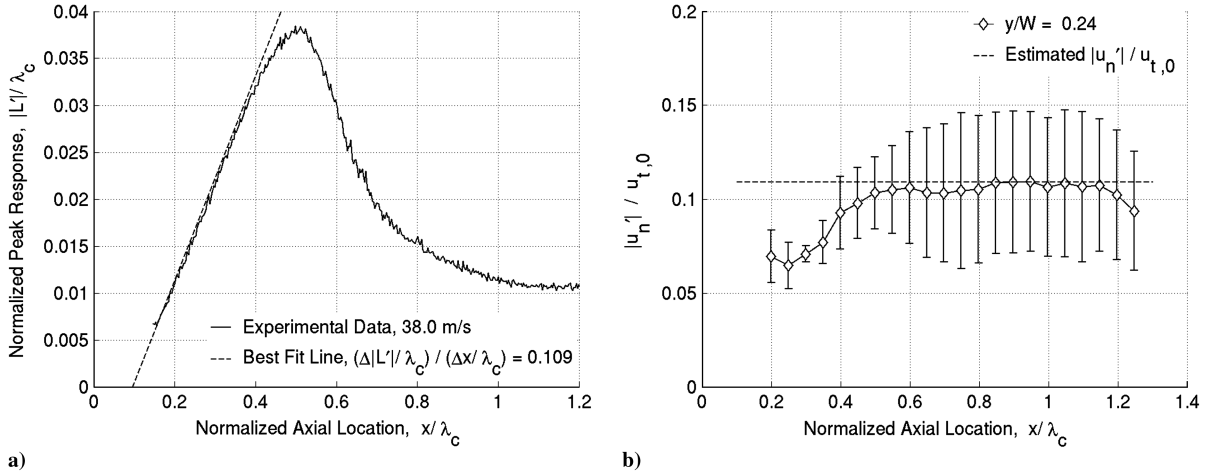

Fig. 17 Part a) normalized flame edge amplitude and best-fit line to the initial linear region. Part b) ratio of transverse velocity amplitude to mean axial velocity as a function of downstream distance. The slope of the best-fit line from part a is the dashed line. The excitation voltage is 12 V and the mean flow velocity is 38 m/s.

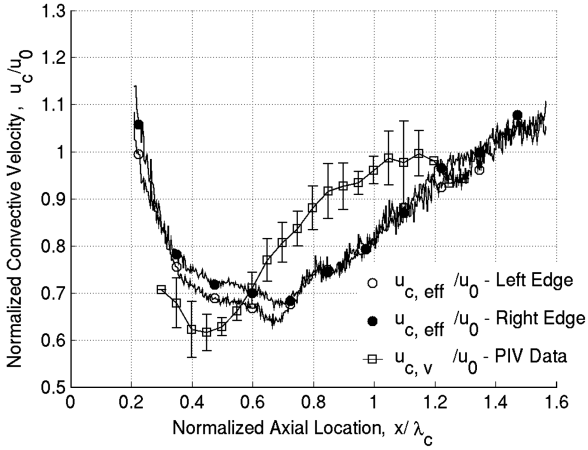

Fig. 18 Slope of the luminosity flame edge and velocity phase data as obtained from Figs. 12 and 19a.

from inspection of Eq. (10) that $u_{c,\text{eff}} > u_{c,v}$ when $u_{c,v} < u_{t,0}\cos\theta$ and vice versa. In the far field, $u_{c,\text{eff}}$ asymptotes to $u_{t,0}\cos\theta$.

Both of these qualitative trends can be seen to be consistent with the phase data shown in Fig. 18. This graph shows that $u_{c,v} < u_o$ and $u_{c,\text{eff}} > u_{c,v}$ in the near field. Furthermore, farther downstream $u_{c,\text{eff}} \sim u_o$.

To evaluate these theoretical results quantitatively, Fig. 19a plots the measured phase characteristics of the transverse perturbation velocity. This value is converted into an inferred convection velocity, $u_{c,v}$, and plotted at several transverse locations in Fig. 19b. Using the measured phase results for the flame wrinkle from Fig. 12 (leading to the average value of $u_{c,f}/u_0 = 0.59$) and Eq. (9), the disturbance velocity convection speed is estimated and indicated in the figure by a dashed line. While the measured velocity convection speeds are higher than the predicted value, they appear to converge to nearly the same value at the flame holder lip, which is where the theoretical expression is valid.

Taken together, the above two results show that a reasonable quantitative agreement can be obtained for the near-field flame gain and phase. The far-field flame response characteristics are now considered. Here, only qualitative comparisons are possible, due to the sensitivity of the flame results to threshold I_t.

The axial location at which the flame response peaks, x_{peak}, is examined first. This axial location cannot be precisely determined from the data since it is a function of the threshold level, but evaluation of this location at several I_t values suggests it lies between $0.4 < x_{\text{peak}}/\lambda_c < 0.6$ (see Fig. 9a). Simple theoretical calculations of x_{peak} cannot be developed, because x_{peak} depends upon amplitude of perturbation and the detailed character of the velocity field. However, an approximate expression for x_{peak} can be derived using wave interference arguments, as shown in Shin et al. [32]. Since flame excitation and flame response disturbances do not propagate at the same speed [as can be inferred from Eq. (10)], they lead to constructive and destructive interference along the flame [32]. The location of x_{peak} approximately coincides with the point where they constructively superpose with each other; i.e., where they are in phase. As shown by Shin et al. [32], this leads to the following predicted location for x_{peak}:

$$x_{\text{peak}}/\lambda_c = \frac{\cos^2\theta}{2\left|\frac{u_0}{u_{c,v}}\cos^2\theta - 1\right|} \tag{11}$$

It should be noted that this equation assumes the decay in the exciting vortex is negligible at x_{peak}, which appears to be the case as from Fig. 17b. Using the value of $u_{c,v}/u_0 = 0.48$ (from Fig. 19b), Eq. (11) predicts that $x_{\text{peak}}/\lambda_c = 0.45$. This prediction, indicated by the dashed vertical line in Fig. 20, is in good agreement with the data. Note that when $u_{c,v} \sim u_0$, the sensitivity of x_{peak} to parameter values and uncertainties is very large, making it more difficult to accurately predict.

Finally, the region of the flame farther downstream of the peak is examined. Here, the dependency of the flame results upon threshold is more significant, so discussion is limited to simply comparing the general features of the model and measurements. Moreover, because of the large magnitude of flame-front fluctuations, it is difficult to determine the instantaneous conditional velocity at the flame from measurements. For this reason, a modeled velocity disturbance profile is used. It is known that acoustic excitation results in a train of convecting vortices generated in the bluff body shear layer that decay in the downstream direction [35]. As such, the axial velocity field is modeled by the equation:

$$u(x, y, t) = u_0 \tag{12}$$

$$v(x, y, t) = \varepsilon \cdot \cos(\omega(t - x/u_{c,v})) \tag{13}$$

where ε denotes the disturbance amplitude. The full nonlinear G-equation is solved numerically. Performing these calculations requires specifying all model parameters described earlier ($\theta = 6°$, $\varepsilon = 0.11$, $f_0 = \omega/2\pi = 250$ Hz, and $u_{c,v}/u_0 = 0.48$). The parameters $u_{c,v}/u_0$ and ε are determined from Figs. 17 and 19, respectively.

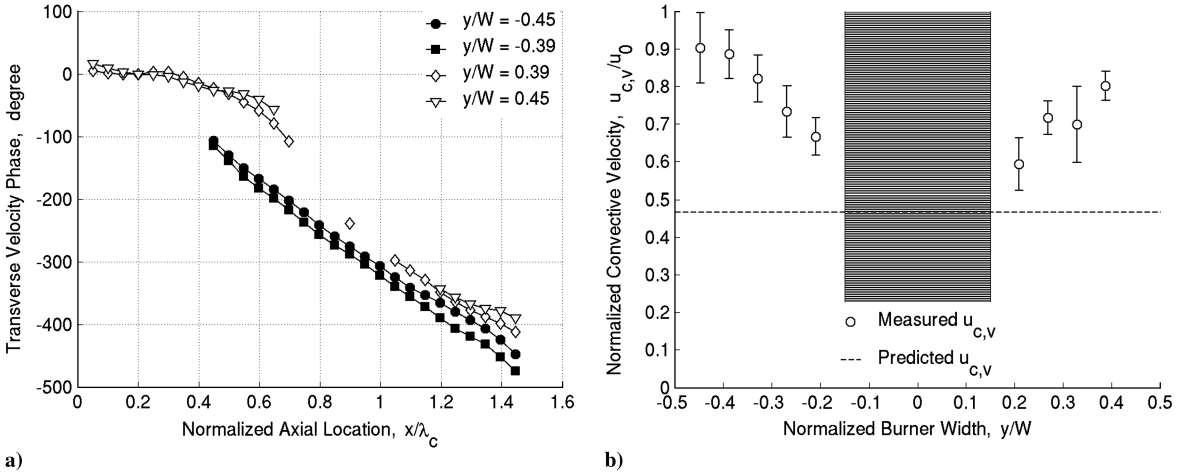

Fig. 19 Part a) transverse velocity phase as a function of axial distance for one realization. Points where $R^2 < 0.4$ (goodness-of-fit parameter of a sine wave to the time series) are disregarded. To calculate the convective velocity, a straight line is fitted to each y/W location (only points where $R^2 > 0.99$ are considered). Open symbols represent the left flame edge while the filed in symbols represent the right flame edge. Part b) convective velocity calculated from the phase of velocity fluctuations in part a, normalized by the mean axial velocity. The dashed line is the prediction from Eq. (10). Error bars represent 1 standard deviation and the area directly behind the bluff body is shown by the gray rectangle. The excitation voltage is 12 V and the mean flow velocity is 38 m/s.

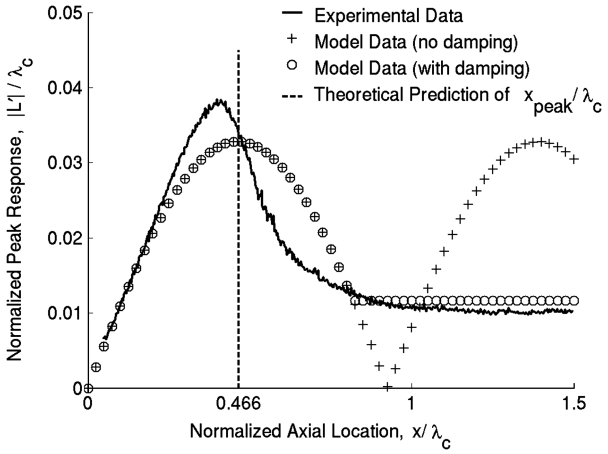

Fig. 20 Comparison of experimentally measured and theoretically calculated flame edge response at $u_0 = 38$ m/s and 12 V excitation voltage. x_{peak} location is predicted by Eq. (11). Model data conditions: $u_{c,v}/u_o = 0.48$, $\beta = 7.0$, $\varepsilon = 0.11$.

Figure 20 overlays a theoretical calculation of gain response curve predictions with the data. Comparison of these predictions with the measurements shows similar results in the initial rise, peak, then decay of the flame response.

Although computational results predict a second peak (indicated by + in Fig. 20), this is not observed experimentally. This theoretically predicted second peak can be largely suppressed by damping the vortical disturbance in the far field. For example, the figure also plots (shown as *o* in Fig. 20) results from a two-section, piecewise constant velocity perturbation model, where $\varepsilon = 0.11$ and 0 for $x/\lambda_c < 0.82$ and $x/\lambda_c > 0.82$, respectively. As shown, this model result very closely captures the far-field flame response.

This latter model does not appear to describe the actual velocity perturbation field, as can be seen from Fig. 17, however, illustrating some shortcomings of the theory for predicting far-field flame characteristics. In other words, using the actual measured velocity field suggests that there should be a continued oscillation in flame gain, associated with interfering waves on the flame progressively moving in and out of phase with downstream distance. This is not observed experimentally, suggesting that flame wrinkles are dissipated more rapidly than predicted.

It is speculated that this is due to the model not fully capturing turbulent flame effects. Dissipation of flame wrinkles occurs due to flame propagation normal to itself. The theory is essentially a quasi-laminar theory (i.e., simply replacing S_L in Eq. (1) with some inferred S_T based the measured flame angle); as such, flame propagation occurs normal to the time-averaged flame brush at this inferred turbulent flame speed. However, as noted by Hemchandra et al. [36], fine-scale turbulent wrinkling causes much more rapid dissipation of periodic flame wrinkles than predicted from such considerations. This suggests that a more explicit incorporation of turbulent effects into the harmonically forced flame problem is required to understand the far-field evolution of the flame.

IV. Conclusions

This paper characterizes key parameters influencing the spatio-temporal response of an acoustically excited bluff body flame. Data and modeling results show that the flame response magnitude rises, peaks and then decays with downstream location. The phase of the flame response exhibits an essentially linearly decreasing dependence upon axial location. The kinematic model shows that the key processes controlling the response are 1) the anchoring of the flame at the bluff body, 2) the excitation of flame-front wrinkles by the oscillating velocity, 3) interference of two characteristic waves, and 4) flame propagation normal to itself at the local flame speed. The first two processes control the initial growth and the last two processes control the peak and subsequent decay of the flame response.

These measurements and understanding provide guidance for future experimental work. First, future measurements would benefit from laser sheet imaging to characterize the flame edge, as done in our earlier studies [24–26]. Second, they show that resolution of the bluff body near field is critical to verify the flame anchoring, which plays such an important role in the flame's near-field response character. They also show provisions for increased downstream viewing will be needed to capture the decay region at the highest flow velocities. Finally, they show that accurate characterization of the vortex amplitude, propagation speed, and decay rate are needed to understand the sources of flame excitation.

Appendix: Derivations of Eqs. (3), (4), (7), and (8)

A. Derivation of Eqs. (3) and (4)

Substituting $G = y - L(x,t)$ into Eq. (1) leads to:

$$\frac{\partial L}{\partial t} + u\frac{\partial L}{\partial x} - v = s_L\sqrt{1+\left(\frac{\partial L}{\partial x}\right)^2} \tag{A1}$$

Decompose the flame position and velocities into temporal mean and fluctuation part as follows:

$$L = L_0(x) + L'(t,x) \qquad u = u_0(x) + u'(t,x)$$
$$v = v_0(x) + v'(t,x) \tag{A2}$$

Then, substituting the above decompositions into Eq. (A1) and collecting the first-order terms leads to:

$$\frac{\partial L'}{\partial t} + \cos\theta \cdot u_{t,0}\frac{\partial L'}{\partial x} = \frac{u'_n}{\cos\theta} \tag{A3}$$

where $\theta, u_{t,0}$, and u'_n are local flame angle, mean velocity tangential to the flame front, and fluctuation velocity normal to the flame front, respectively.

B. Derivation of Eq. (7)

At the flame attachment point $x = 0$, Eq. (4) [which is the same as Eq. (A3)] satisfies $L'(t) = 0$, or $\mathrm{d}L'/\mathrm{d}t = 0$. Taking the absolute value of the remaining terms and noting that $|\partial L'/\partial x| = \partial|L'|/\partial x$ because $L'(t) = 0$, leads to:

$$\frac{\partial|L'|}{\partial x} = \frac{|u'_n|}{u_{t,0}}\frac{1}{\cos^2\theta} \tag{B1}$$

C. Derivation of Eq. (8)

We expand the velocity fluctuation of Eq. (4) [which is the same as Eq. (A3)] using Taylor series and assume the form of solution L':

$$\frac{u'_n(x,t)}{\cos\theta} = \mathrm{Re}[(a_0 + a_1 x + \cdots)\cdot \exp^{i\omega(t-\frac{x}{u_{c,v}})}] \tag{C1}$$

$$L'(x,t) = \mathrm{Re}[|\hat{L}'(x)|e^{i\{\omega t + \phi_f(x)\}}] \tag{C2}$$

Expanding the solution of Eq. (4) around $x = 0$ subject to the boundary conditions there leads to:

$$|\hat{L}'(x)| = \frac{a_0}{u_{t,0}\cdot\cos\theta}x + \frac{a_1}{2u_{t,0}\cdot\cos\theta}x^2 + \mathcal{O}(x^3) \tag{C3}$$

$$\phi_f(x) = -\frac{1}{2}\left(\frac{\omega}{u_{c,v}} + \frac{\omega}{u_{t,0}\cdot\cos\theta}\right)x$$
$$-\frac{a_1}{12a_0}\left(\frac{\omega}{u_{c,v}} - \frac{\omega}{u_{t,0}\cdot\cos\theta}\right)x^2 + \mathcal{O}(x^3) \tag{C4}$$

Therefore, the phase slope can be derived as follows:

$$\left.\frac{\partial\phi_f}{\partial x}\right|_{x=0} = -\frac{1}{2}\left(\frac{\omega}{u_{c,v}} + \frac{\omega}{u_{t,0}\cdot\cos\theta}\right) \tag{C5}$$

Acknowledgment

This work was partially supported by the U.S. Air Force, Barry Kiel, Contract Monitor (Contract FA-8650-07-M-2784).

References

[1] Smith, D. A., and Zukoski, E. E. "Combustion Instability Sustained by Unsteady Vortex Combustion," *21st AIAA/ASME/SAE/ASEE Joint Propulsion Conference and Exhibit*, AIAA Paper 85-1248, 1985.

[2] Hegde, U. G., Reuter, D., Daniel, B. R., and Zinn, B. T. "Flame Driving of Longitudinal Instabilities in Dump Type Ramjet Combustors," *Combustion Science and Technology*, Vol. 55, No. 4, 1987, pp. 125–138.
doi:10.1080/00102208708947075

[3] Poinsot, T. J., Trouve, A. C., Veynante, D. P., Candel, S. M., and Esposito, E. J. "Vortex-Driven Acoustically Coupled Combustion Instabilities," *Journal of Fluid Mechanics*, Vol. 177, 1987, pp. 265–292.
doi:10.1017/S0022112087000958

[4] Yu, K. H., Trouvé, A., and Daily, J. W., "Low-Frequency Pressure Oscillations in a Model Ramjet Combustor," *Journal of Fluid Mechanics*, Vol. 232, 1991, pp. 47–72.
doi:10.1017/S0022112091003622

[5] Williamson, C. H. K., "Vortex Dynamics in the Cylinder Wake," *Annual Review of Fluid Mechanics*, Vol. 28, 1996, pp. 477–539.
doi:10.1146/annurev.fl.28.010196.002401

[6] Prasad, A., and Williamson, C. H. K., "The Instability of the Shear Layer Separating from a Bluff Body," *Journal of Fluid Mechanics*, Vol. 333, 1997, pp. 375–402.
doi:10.1017/S0022112096004326

[7] Cimbala, C. M., "Large Structure in the Far Wakes of Two-Dimensional Bluff Bodies," Ph.D., Thesis, California Inst. of Technology, Pasadena, CA, 1984.

[8] Perry, A. E., Chong, M. S., and Lim, T. T., "The Vortex Shedding Process Behind Two-Dimensional Bluff Bodies," *Journal of Fluid Mechanics*, Vol. 116, 1982, pp. 77–90.
doi:10.1017/S0022112082000378

[9] Huerre, P., and Monkewitz, P. A., "Local and Global Instabilities in Spatially Developing Flows," *Annual Review of Fluid Mechanics*, Vol. 1, 1990, pp. 473–537.
doi:10.1146/annurev.fl.22.010190.002353

[10] Sheridan, J., Soria, J., Wu, J., and Welsh, M. C., "The Kelvin–Helmholtz Instability of the Separated Shear Layer from a Circular Cylinder," *IUTAM Symposium*, Springer Academic Publishers, Dordrecht, The Netherlands, 1992.

[11] Erickson, R. R., Soteriou, M. C., and Mehta, P. G., "The Influence of Temperature Ratio on the Dynamics of Bluff Body Stabilized Flames," *44th AIAA Aerospace Sciences Meeting and Exhibit*, AIAA Paper 2006-753, 2006.

[12] Hermanson, J. C., and Dimotakis, P. E., "Effects of Heat Release in a Turbulent, Reacting Shear Layer," *Journal of Fluid Mechanics*, Vol. 199, 1989, pp. 333–375.
doi:10.1017/S0022112089000406

[13] McMurtry, P. A., Riley, J. J., and Metcalfe, R. W., "Effects of Heat Release on the Large-Scale Structure in Turbulent Mixing Layers," *Journal of Fluid Mechanics*, Vol. 199, 1989, pp. 297–332.
doi:10.1017/S002211208900039X

[14] Soteriou, M. C., and Ghoniem, A. F., "The Vorticity Dynamics of an Exothermic, Spatially Developing, Forced Reacting Shear Layer," *Proceedings of the Combustion Institute*, Vol. 25, No. 1, 1994, pp. 1265–1272.
doi:10.1016/S0082-0784(06)80767-8

[15] Wu, M. S., and Driscoll, J. F., "A Numerical Simulation of a Vortex Convected Through a Laminar Premixed Flame," *Combustion and Flame*, Vol. 91, Nos. 3–4, 1992, pp. 310–322.
doi:10.1016/0010-2180(92)90060-3

[16] Sinibaldi, J. O., Mueller, C. J., Tulkki, A. E., and Driscoll, J. F., "Suppression of Flame Wrinkling by Buoyancy: The Baroclinic Stabilization Mechanism," *AIAA Journal*, Vol. 36, No. 8, 1998, pp. 1432–1438.
doi:10.2514/2.534

[17] Louch, D. S., and Bray, K. N. C., "Vorticity in Unsteady Premixed Flames: Vortex Pair–Premixed Flame Interactions Under Imposed Body Forces and Various Degrees of Heat Release and Laminar Flame Thickness," *Combustion and Flame*, Vol. 125, No. 4, 2001, pp. 1279–1309.
doi:10.1016/S0010-2180(00)00128-0

[18] Ducruix, S., Schuller, T., Durox, D., and Candel, S., "Combustion Dynamics and Instabilities: Elementary Coupling and Driving Mechanisms," *Journal of Propulsion and Power*, Vol. 19, No. 5, 2003, pp. 722–734.
doi:10.2514/2.6182

[19] Preetham, Thumuluru, S. K., and Lieuwen, T., "Linear Response of Premixed Flames to Flow Oscillations: Unsteady Stretch Effects," *AIAA Aerospace Sciences Meeting and Exhibit*, AIAA Paper 2007-0176, 2007.

[20] Schuller, T., Durox, D., and Candel, S., "A Unified Model for the Prediction of Laminar Flame Transfer Functions Comparisons Between Conical and *V*-Flame Dynamics," *Combustion and Flame*, Vol. 134, Nos. 1–2, 2003, pp. 21–34.
doi:10.1016/S0010-2180(03)00042-7

[21] Preetham, and Lieuwen, T., "Nonlinear Flame-Flow Transfer Function Calculations: Flow Disturbance Celerity Effects," *40th AIAA/ASME/SAE/ASEE Joint Propulsion Conference & Exhibit*, AIAA Paper 2004-4035, 2004.

[22] Preetham, and Lieuwen, T., "Nonlinear Flame-Flow Transfer Function Calculations: Flow Disturbance Celerity Effects Part 2," *43rd AIAA Aerospace Sciences Meeting & Exhibit*, AIAA Paper 2005-0543, 2005.

[23] Peters, N., *Turbulent Combustion*, Cambridge Univ. Press, Cambridge, England, 2000.

[24] Shanbhogue, S. J., and Lieuwen, T., "Response of a Rod Stabilized, Premixed Flame to Longitudinal Acoustic Forcing," *ASME Turbo Expo: Power for Land, Sea and Air*, American Society of Mechanical Engineers Paper GT-2006-90302, 2006.

[25] Shanbhogue, S. J., Shin, D.-H., Hemchandra, S., Plaks, D., and Lieuwen, T., "Flame-sheet dynamics of bluff-body stabilized flames using longitudinal acoustic forcing," *Proceedings of the Combustion Institute*, Vol. 32, No. 2, 2009, pp. 1787–1794.
doi:10.1016/j.proci.2008.06.034. doi

[26] Shanbhogue, S. J., Plaks, D., Nowicki, G., Preetham, and Lieuwen, T., "Response of Rod Stabilized Flames to Harmonic Excitation: Shear Layer Rollup and Flame Kinematics," *42nd AIAA/ASME/SAE/ASEE Joint Propulsion Conference & Exhibit*, AIAA Paper 2006-5232, 2006.

[27] Brown, C. T., McDonell, V. G., and Kiel, B., "Test Bed for Characterization of Liquid Jet Injection Phenomenon at Augmentor Conditions," *42nd AIAA/ASME/SAE/ASEE Joint Propulsion Conference and Exhibit*, AIAA Paper 2006-4569, 2006.

[28] Fleifil, M., Annaswamy, A. M., Ghoneim, Z. A., and Ghoneim, A. F., "Response of a Laminar Premixed Flame to Flow Oscillations: A Kinematic Model and Thermoacoustic Instability Results," *Combustion and Flame*, Vol. 106, No. 4, 1996, pp. 487–510.
doi:10.1016/0010-2180(96)00049-1.

[29] Ducruix, S., Durox, D., and Candel, S., "Theoretical and Experimental Determination of the Transfer Function of a Laminar Premixed Flame," *Proceedings of the Combustion Institute*, Vol. 28, No. 1, 2000, pp. 765–773.
doi:10.1016/S0082-0784(00)80279-9

[30] Yang, V., and Culick, F. E. C., "Analysis of Low Frequency Combustion Instabilities in a Laboratory Ramjet Combustor," *Combustion Science and Technology*, Vol. 45, No. 1, 1986, pp. 1–25.
doi:10.1080/00102208608923839

[31] Lieuwen, T., "Physics of Premixed Combustion: Acoustic Wave Interactions," *Combustion Instabilities in Gas Turbine Engines: Operational Experience, Fundamental Mechanisms, and Modeling*, AIAA, Reston, VA, 2005.

[32] Shin, D. H., Shanbhogue, S. J., and Lieuwen, T., "Premixed Flame Kinematics in an Axially Decaying, Harmonically Oscillating Vorticity Field," *44th AIAA/ASME/SAE/ASEE Joint Propulsion Conference & Exhibit*, AIAA Paper 2008-5042, 2008.

[33] Jiang, G., and Peng, D., "Weighted ENO Schemes for Hamilton–Jacobi Equations," *SIAM Journal on Scientific Computing*, Vol. 21, No. 6, 2000, pp. 2126–2143.
doi:10.1137/S106482759732455X

[34] Gottlieb, S., and Shu, C., "Total Vatiation Diminishing Runge–Kutta Schemes," *Mathematics of Computation*, Vol. 67, 1998, pp. 73–85.
doi:10.1090/S0025-5718-98-00913-2

[35] Shanbhogue, S. J., and Lieuwen, T., "Studies on the Vorticity Field of Harmonically Excited Bluff Body Flames," *46th AIAA Aerospace Sciences Meeting and Exhibit*, AIAA Paper 2009-22, 2008.

[36] Hemchandra, S., Preetham, and Lieuwen, T., "Response of Turbulent Premixed Flames to Harmonic Acoustic Forcing," *Proceedings of the Combustion Institute*, Vol. 31, No. 1, 2007, pp. 1427–1434.
doi:10.1016/j.proci.2006.07.198. doi

A. Gupta
Associate Editor